Measurement of Thermomechanical Motion in the Few-Phonon Regime Using Carbon Nanotube Charge Sensors

Julie ElDik

Supervised by: Stefan Forstner and Adrian Bachtold

The Institute of Photonic Sciences, 08860 Barcelona

22 August 2025

We report the detection of thermomechanical motion in suspended carbon nanotube (CNT) resonators operating in the few-phonon regime, using an integrated charge sensor at cryogenic temperatures. We fabricate ultra-clean single-walled CNTs using a chemical vapor deposition (CVD) method and suspend them across predefined gate and electrode structures. The devices allow confinement of single and double quantum dots electrostatically defined in a CNT and capacitively coupled to a nearby charge sensor quantum dot. A radio-frequency (RF) readout circuit enables sensitive detection of thermomechanical motion at mode temperatures as low as 50 mK, corresponding to an average phonon occupation number below 10. We observe Lorentzian power spectral densities of the mechanical resonance and track the evolution of displacement amplitude with temperature. Deviations from ideal thermal scaling suggest additional temperature-dependent effects not fully captured by charge sensor sensitivity alone. These results aim to improve quantum nanomechanical sensing.

Keywords: Quantum nanomechanics, quantum dot, carbon nanotube, charge stability diagrams, deep learning, charge sensing.

Julie ElDik: julie.eldik@gmail.com

Acknowledgements

I would like to sincerely thank Adrian Bachtold for giving me the great opportunity to join his group and contribute to his projects. I am deeply grateful to Stefan, one of the most brilliant people I have met, for his invaluable support and constant encouragement, thank you for being an exceptional mentor and a friend to me. To my team members, thank you for your unconditional support and kindness, especially to Marta and Eva, with whom I had the pleasure of working closely on this project.

I am also deeply thankful to my brother, grandmother, and family, who encouraged my love for science from an early age. Finally, to my friends here, thank you for giving me a home in Barcelona.

Contents

1 Introduction and Background

1.1 Motivation

Over the past decade, nanomechanical oscillators have emerged as key components in quantum technologies and precision sensing. Their high frequencies and extreme sensitivity to external perturbations make them ideal for detecting minute forces, masses, and fields [CB12, JZ08], providing a platform for coupling to diverse physical phenomena, ranging from the tidal forces generated by gravitational waves [AC16] to quantum transitions between electronic states [CR98]. Among these devices, carbon nanotubes (CNTs) stand out as the lightest and among those with the highest aspect ratios, enabling the most sensitive force measurements ever achieved with a mechanical resonator [SLdBB18].

When used to define gate-controlled quantum dots, CNTs offer unprecedented capabilities for probing strongly correlated electron systems and exploring quantum states in mesoscopic regimes [MJBM05]. Owing to their extremely low mass, CNT resonators exhibit large zero-point displacement amplitudes in the picometer range [CGS12], which makes it possible to reach ultra-strong coupling regime, where the coupling strength surpass both the mechanical resonance frequency and dominant sources of dissipation [MB13, FVA22].

In this project, we investigate suspended CNT devices that integrate quantum dots with the motion of nanomechanical resonators. We grow the nanotube using Chemical Vapor Deposition "Fast-heating" method [HL04] . We introduce a CNT-based charge sensor that leverages radio-frequency (RF) readout, enabling ultra-precise detection of mechanical motion. This allows the observation of thermomechanical motion down to a mode temperature of 50 mK, which corresponds to an average thermal phonon occupation number below 10. Lastly, we study the temperature dependence of thermomechanical motion.

1.2 Carbon Nanotubes

Structurally, a carbon nanotube is a rolled-up sheet of graphene forming a hollow cylinder. The geometry of this roll-up is described by a chirality vector (n, m), which determines the electronic properties of the tube. Quantization of electron wavevectors around the nanotube circumference produces discrete lines in the graphene Brillouin zone. When these lines intersect the Dirac points (K or K'), the nanotube exhibits metallic behavior; otherwise, a bandgap forms and the nanotube is semiconducting. The chiral indices (n, m) set the orientation and spacing of these quantization lines, with armchair nanotubes ($n = m$) always metallic, and zigzag or chiral types varying between metallic and semiconducting depending on their geometry. Depending on this chirality, CNTs can behave either as metallic conductors or as semiconductors with a tunable band gap [EALK15, PAW03].

Two major types of CNTs are distinguished: single-walled carbon nanotubes (SWCNTs), which consist of a single layer of graphene, and multi-walled carbon nanotubes (MWCNTs), composed of multiple concentric graphene cylinders [Iij91]. SWCNTs are especially valuable in quantum device applications due to their well-defined electronic states and simpler energy spectrum [EALK15].

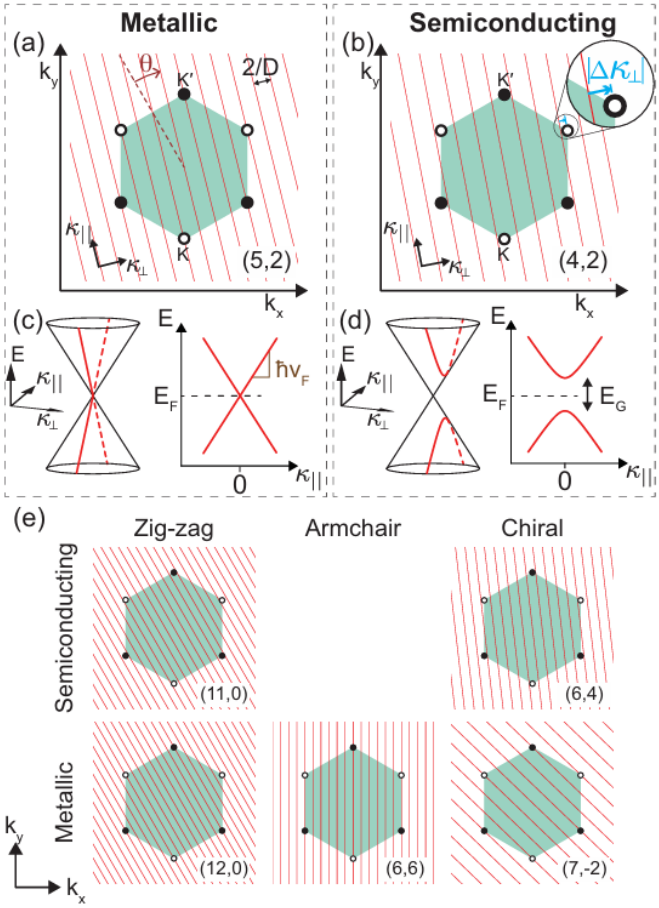

Figure 1: Figure adapted from E .Laird et al. [EALK15] shows a schematic of chirality and its influence on CNT electronic properties. The orientation of quantization lines in the graphene Brillouin zone determines whether a CNT is metallic or semiconducting.

Despite these advantages, the use of CNTs in high-precision sensing faces several technical challenges. Electronic thermal fluctuations impose limits on displacement resolution, while the small amplitudes of both mechanical and electrical signals demand extremely sensitive readout techniques. Other environmental coupling, such as tunnel broadening of energy levels [EALK15], interactions with two-level systems (TLS) [MSN25] and quantum back-action [SSM25] can further degrade signal fidelity and sensitivity. Furthermore, device variability caused by uncontrolled chirality, fabrication-induced disorder, and environmental perturbations can hinder reproducibility [EALK15].

1.3 Structure of the Thesis

This thesis is organized as follows. In Chapter 2, we introduce the device architecture and describe the procedure we used to grow ultra-sensitive semiconducting SWCNTs. In Chapter 3, we describe the formation of single and double quantum dots, and present the cryogenic charge-sensing readout technique. Chapter 4 focuses on our measurements of the nanotube's thermal motion, detailing the temperature dependence of the power spectral density and the analysis of asymmetries. Chapter 5 summarizes the main results. Appendix A details the architecture, training strategy, and performance analysis of the deep learning model developed to learn from charge stability diagrams in gate-defined quantum dot devices.

2 Carbon Nanotube Fabrication

2.1 CNT Device Architecture

The devices used in this study consist of SWCNT integrated with multiple local gates for precise electrostatic control. Each device includes two source electrodes, one drain electrode with a narrow width, and six gate electrodes. Gates 1–5 are employed to define and tune either single or double quantum dots by applying appropriate voltages. This allows fine control over the electron occupation, tunnel barriers, and interdot coupling.

The sixth gate, positioned between the left source and the drain, defines an independent quantum dot that serves as a charge sensor for readout. The gate geometry is optimized to ensure strong capacitive coupling to the CNT while maintaining high spatial resolution for accurate quantum dot definition and effective coupling to the charge sensor.

A representative scanning electron microscope (SEM) image is shown in Fig. 2, highlighting the suspended CNT, gate array, and contact configuration.

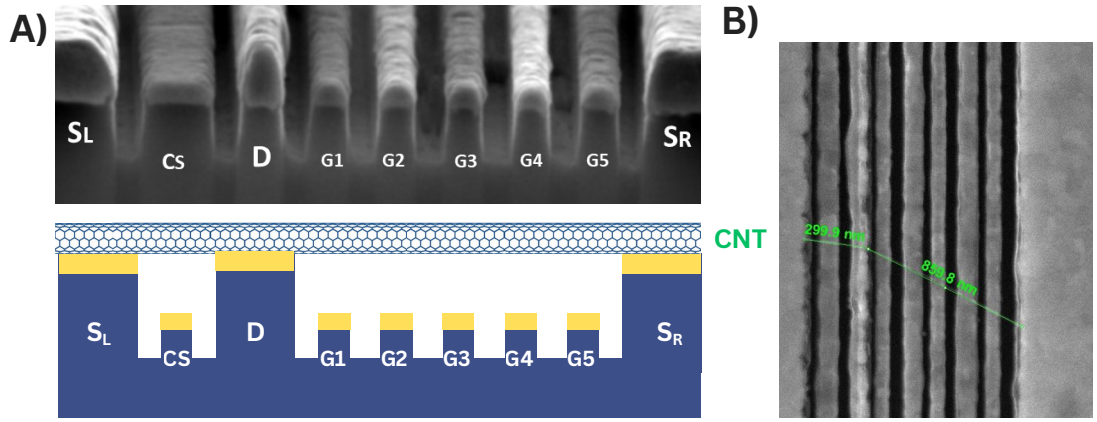

Figure 2: (A) Side view of the gate geometry: SEM image (top) and schematic (bottom). (B) Top view of the device with the suspended CNT highlighted in green.

2.2 Initial Wafer Preparation

Producing an atomically clean suspended CNT devices calls for a careful, step-by-step approach to keep conditions stable and prevent contamination or damage to the nanotubes. The aim is to have CNTs suspended across electrodes, providing a structure suitable for sensitive measurements. To summarize the process, nanotube growth is carried out directly on the substrates using an Fe/Mo catalyst and Chemical Vapor Deposition (CVD) at 1050 °C in an $Ar/H_2/CH_4$ environment.

The process begins with pre-patterned chips provided by our collaborator David Czaplewski at Argonne National Laboratory (ANL). These chips already contain electrodes and etched trenches that define the device layout. The process starts with a high-resistivity silicon wafer, selected to suppress leakage currents and provide strong electrical isolation. A thin film of poly(methyl methacrylate) (PMMA) is then added on top, serving as a sacrificial layer that is later removed during the process. The source, drain, and gate electrodes have a 100 nm layer of platinum on top of a 5 nm titanium layer.

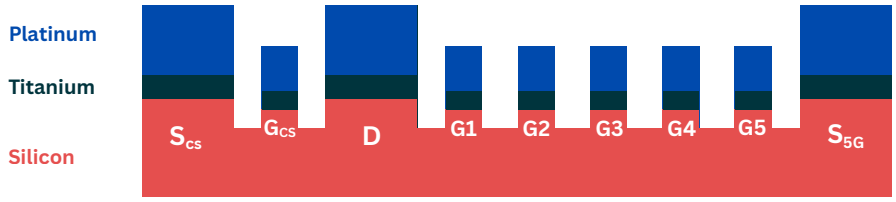

Figure 3: Side view schematic of the device structure after fabrication.

2.3 CNT Synthesis By Chemical Vapor Deposition

Carbon nanotube (CNT) growth begins with the preparation of a catalyst solution that is deposited on the chip surface. It is made from Iron (Fe) catalyst nanoparticles combined with molybdenum (Mo) in an Aluminum Oxide Matrix. The solution is sonicated for at least 10 minutes to ensure that the nanoparticles are well dispersed. This step is important for achieving consistent CNT growth across the substrate. Before the catalyst is applied, the chip is exposed to oxygen plasma for one minute, which removes any remaining organic contaminants and improves the adhesion of the catalyst.

A droplet of 10 μL of the sonicated solution is placed at the center of the chip and left to air dry. This process results in a nearly uniform distribution of catalyst particles. Excess catalyst is removed everywhere except on the source and drain islands, in a lift-off step in which the chip is immersed in acetone at 50 °C for 90 minutes, which dissolves the PMMA sacrificial layer. The chip is then transferred to a fresh beaker of cold acetone, rinsed in 2-propanol, and dried using a nitrogen gun. In this study a one-to-ten volume dilution of the catalyst solution was used to control catalyst density and to optimize CNT growth conditions.

In the CVD process, CNTs are produced by decomposing carbon-rich methane (CH_4) in the presence of catalyst nanoparticles. Growth is performed in a Lindberg Blue tube furnace using the fast heating method. In this approach the furnace is quickly brought to 1050 °C while argon (Ar) and hydrogen (H_2) flow continuously. Once the desired temperature is reached, the samples are placed inside the furnace. The temperature is then reduced to 900 °C and nanotube growth proceeds for six minutes while H_2 flows at 100 sccm, Ar at 500 sccm, and CH_4 at 550 sccm.

When growth is complete, the next step is to identify which devices contain nanotubes that are properly suspended between the charge sensor source (S_{cs}) and the 5-gate source (S_{5G}) electrodes, while also making contact with the drain electrode, without touching the gates.

Because nanotube growth is inherently random, the yield is statistical. A typical chip contains about 40 devices, and the goal is to obtain at least one with a defect-free, suspended CNT that meets all functional requirements: it must grow across the gate array, be single-walled and semiconducting, and include only one nanotube across the gate structure. Device screening is carried out in two steps, first by probing in air and then by probing in vacuum.

2.4 Device Characterization

The first stage of device testing is air probing, which is carried out at room temperature and atmospheric pressure to verify CNT growth and to check for electrical shorts. Devices that meet this criterion are then measured in a vacuum probe station at a pressure of about 6

μbar and room temperature. Measurements in vacuum reduce the risk of ionization events that could damage the nanotube and allow more sensitive characterization, making it possible to identify devices that display the gate-voltage dependent conductance expected for a small-gap semiconducting CNT.

Several outcomes indicate failure during either probing method. These include an open circuit with no measurable current between S_{cs} and $S_{5\text{G}}$ (large resistances above 200 $M\Omega$), or leakage currents between neighboring gates or between a gate and the source or drain electrodes. Leakage may result from a collapsed nanotube (often yielding a 100 $k\Omega$-range leak), or a fabrication defect causing a low-resistance path, or from amorphous carbon deposits that usually lead to high-resistance leakage.

Fig. 4 shows the configuration for air probing. Two metallic probes contact the electrode pads connected to the CNT. A low-amplitude voltage sweep from -10 mV to $+10$ mV is applied across S_{cs} and $S_{5\text{G}}$. The current passes through the nanotube, then into an amplifier, and is recorded by an analog-to-digital converter (ADC).

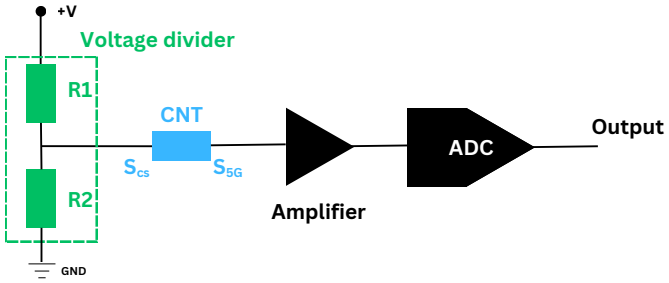

Figure 4: Schematic of the air probing measurement setup.

The configuration for vacuum probing is illustrated in Fig. 5 (A). A low frequency AC signal (typically 19 Hz) with a peak-to-peak amplitude of $V = 20$ mV is applied through a 100 $K\Omega$ resistor connected with the CNT. The gate electrode is used to electrostatically tune the carrier density in the CNT, by sweeping the gate voltage from -2 V to $+2$ V. This allows us to determine whether the CNT behaves as a small-gap semiconductor or as a metallic nanotube.

The CNT resistance is obtained from

$$R_{\text{CNT}} = R\left(\frac{V - V_{\text{meas}}}{V_{\text{meas}}}\right),$$

where R is the parallel resistor and V_{meas} is the voltage drop across it. The Stanford lock-in Amplifier was used to supply and measure the voltage. The conductance, given by the inverse of R_{CNT}, is shown in Fig. 5 (B). The CNT exhibits field-effect transistor-like behavior: sweeping the charge sensor gate (G_{CS}) shifts the CNT Fermi level, yielding hole conduction (p-type) at negative voltages, electron conduction (n-type) at positive voltages, and a conductance minimum when the Fermi level lies within the bandgap.

Leakage current measurements are performed by switching the gate connection from the voltage source to a current-measuring configuration. This setup makes it possible to detect any unintended current paths from a gate to the source, the drain, or other gates, confirming that the gates remain electrically isolated from one another and from the electrodes. Current measured should be on the order of 10 pA to be considered acceptable.

In this study, after growing CNTs, I measured 12 chips in the air probe and 9 devices in the vacuum probe, resulting in 7 good devices. The initially lower-than-expected yield

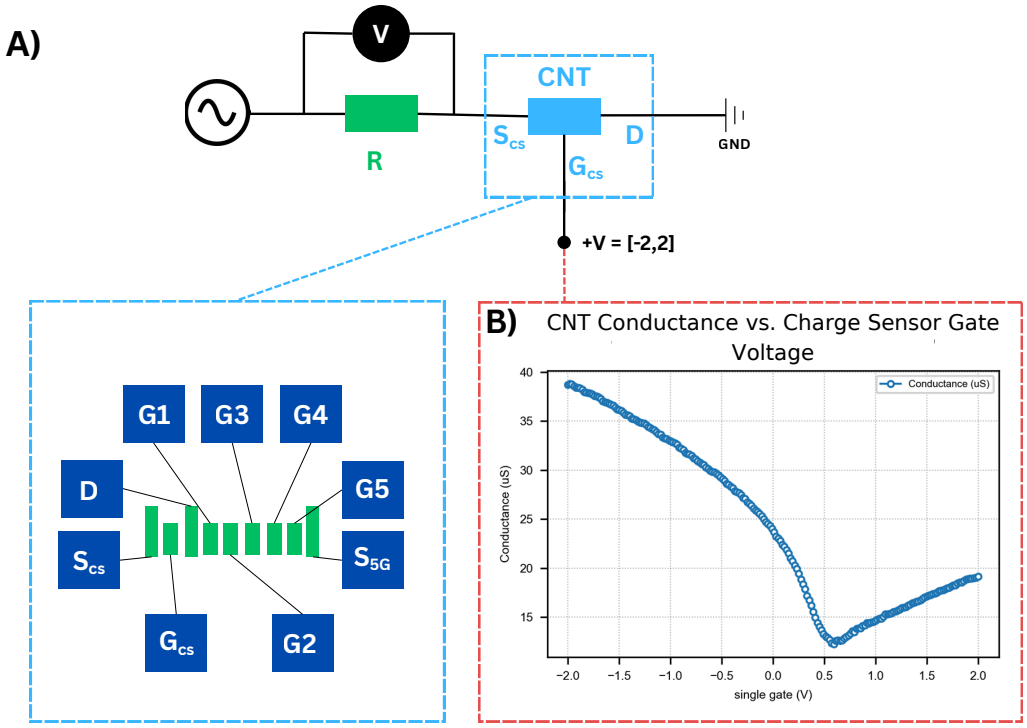

Figure 5: Schematic of the vacuum probing measurement setup.

was traced to a depleted CH_4 gas tank, which caused non-uniform gas flow during growth. Once the issue was identified, the yield was approximately one good device per chip, which is consistent with our expectations. The most common failure mode during air probing was open circuits with resistances above 200 MΩ, while in vacuum probing the main failure was leakage. I also trained a student intern to use these measurement techniques.

3 Device Physics and Experimental Setup

3.1 Single Quantum Dot in Carbon Nanotubes

Quantum dots (QDs) in CNTs are formed using electrostatic gates that locally modulate the potential along the tube, confining carriers into discrete regions [MJBM05]. In our device, a single quantum dot (SQD), as shown in Fig. 7 (A) is defined by two gates that create tunnel barriers, while a central gate tunes the dot's chemical potential. Alternatively, the charge sensor QD can also be defined without dedicated barrier gates, using only the source and drain contacts to provide confinement. At cryogenic temperatures, electrostatic confinement yields discrete, atom-like energy levels, hence the term 'artificial atoms.' Source and drain electrodes at the CNT ends enable transport measurements through the dot [WGvdWK97].

We discuss the energy scales relevant for understanding the physics of quantum transport of electrons in our system. The electrochemical potential for adding the N-th electron in the QD is given by:

$$\mu(N) = \varepsilon_N + E_C\left(N - \tfrac{1}{2}\right) - e\alpha V_g, \tag{1}$$

where

- ε_N is the single-particle orbital energy of the N-th level,
- $E_C = \dfrac{e^2}{C_\Sigma}$ is the charging energy, determined by the total capacitance C_Σ of the dot to source, drain, and gate electrodes,
- V_g is the applied gate voltage,
- $\alpha = \dfrac{C_g}{C_\Sigma}$ is the lever arm, i.e., the fraction of gate voltage that shifts the dot potential.

The addition energy E_{add} is defined as the energy difference between two successive electrochemical potentials:

$$E_{\text{add}}(N) = \mu(N+1) - \mu(N) = E_C + \Delta E, \tag{2}$$

where

$$\Delta E = \varepsilon_{N+1} - \varepsilon_N \tag{3}$$

is the single-particle level spacing. This energy corresponds to the spacing between adjacent Coulomb peaks in transport measurements, which arise when the dot's electrochemical potential aligns with that of the leads, allowing current to flow. Between peaks, current is suppressed due to Coulomb blockade, where electron addition is energetically forbidden [WGvdWK97], as shown in Fig. 6 (A).

The charge sensor relies on the formation of a quantum dot between the charge sensor source (S_{cs}) and drain (D), with the charge sensor gate (G_{cs}) tuning the dot's energy levels. When the energy level of the dot aligns with the Fermi level of the leads, current can flow, resulting in a Coulomb peak in conductance as a function of charge sensor gate voltage, $G(V_g)$, as shown in Fig. 6 (C). On the steep slope of this peak, we define a set point where the conductance is very sensitive to small shifts in the dot's energy level, and we take advantage of this sensitivity in our read-out method, explained in Section 3.3.

The Coulomb peak shape is mainly determined by how energy levels in the quantum dot are broadened, either by temperature or by tunnel coupling to the leads. Additional asymmetries may arise, for example from finite bias effects, or from the presence of a parasitic dot in series.

Tunnel broadening originates from the coupling of the dot to the leads through the tunnel barriers. Because electrons can escape the dot with a characteristic rate Γ, their finite lifetime leads to an intrinsic linewidth of order $\hbar\Gamma$ [WGvdWK97].

Thermal broadening arises from the Fermi-Dirac distribution of the electrons in the source and drain reservoirs, which smears the energy window for transport over a scale of order $k_B T$. When thermal broadening dominates ($\hbar\Gamma \ll k_B T$), three transport regimes can be distinguished depending on the temperature, the charging energy E_C, and the single-particle level spacing ΔE. When $k_B T \gg E_C$, charge quantization is lost. For $\Delta E \ll k_B T \ll E_C$, many states contribute, giving the classical Coulomb blockade regime. Finally, if $k_B T \ll \Delta E < E_C$, only one or a few discrete levels are involved, defining the quantum Coulomb blockade regime [WGvdWK97].

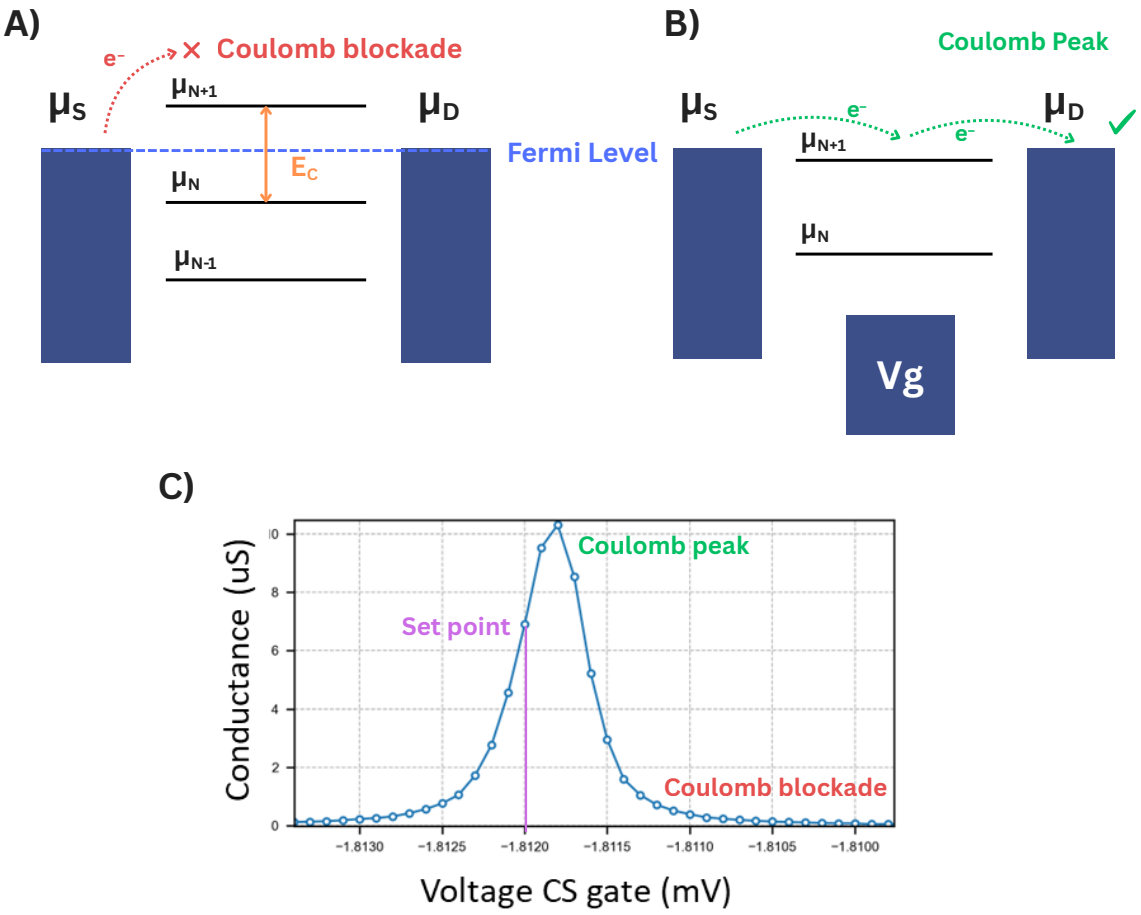

Figure 6: (A) Illustration of Coulomb blockade (B) gate-induced resonant tunneling in a quantum dot. (C) Conductance as a function of gate voltage on the charge sensor quantum dot.

3.2 Double Quantum Dot in Carbon Nanotubes

A double quantum dot (DQD) consists of two confined regions in series along the nanotube, separated by a tunable interdot barrier. Electrostatic gates define each dot independently, allowing full control over their energy levels and occupancy. Each dot is capacitively coupled to its own central gate and to the source or drain electrodes as shown in Fig. 7 (C), while the dots are mutually coupled via a tunnel barrier with capacitance C_m and resistance R_m [WGvdWK02].

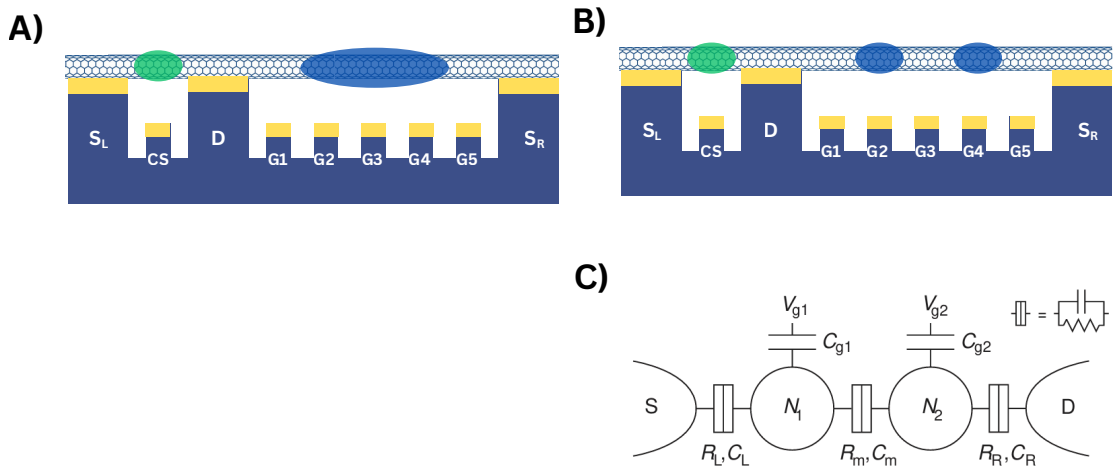

Figure 7: (A) Single quantum dot in the device. (B) Double quantum dot configuration. (C) Figure adapted from W.G. van der Wiel et al. [WGvdWK02] shows the equivalent RC circuit model of two series-coupled quantum dots .

In the capacitance model, the charging energies of the individual dots are

$$E_{C1(C2)} = \frac{e^2}{C_{1(2)}\left(1 - \frac{C_m^2}{C_1 C_2}\right)}$$

where $C_{1(2)}$ is the total capacitances of each dot. The coupling energy between the two dots is

$$E_{Cm} = \frac{e^2}{C_m}.$$

where C_m is the cross-capacitance between the two dots [WGvdWK02].

Transport through a DQD requires three tunneling steps: from the source into a state in the left dot, across the interdot barrier into a state in the right dot, and then into the drain. Resonant transport occurs when the electrochemical potentials μ_{N_L} and μ_{N_R} of the left and right dots are simultaneously aligned with each other and with the leads, giving rise to the characteristic honeycomb charge stability diagram [WGvdWK02], explained in detail in Section 3.4.

When a double quantum dot (DQD) is embedded in a suspended CNT, it can couple to the nanotube's mechanical motion via its flexural vibration mode. When coupled to the flexural mode, the DQD system is described by the Hamiltonian:

$$\hat{H} = \hbar\omega_0 \hat{a}^\dagger \hat{a} + t\,\hat{\sigma}^z + \hbar g_0\,\hat{\sigma}^x \left(\hat{a}^\dagger + \hat{a}\right). \tag{4}$$

The first term, $\hbar\omega_0 \hat{a}^\dagger \hat{a}$, describes the quantized vibrations of the nanotube as a harmonic oscillator with resonance frequency ω_0. The second term, $t\hat{\sigma}^z$, represents the electronic two-level system formed by the left and right charge states of the DQD, with t denoting the tunnel coupling between the two sites. The third term, $\hbar g_0 \hat{\sigma}^x \left(\hat{a}^\dagger + \hat{a}\right)$, captures the electromechanical interaction, where the DQD charge configuration couples to the nanotube's displacement, with coupling strength g_0 [FPB21].

3.3 Cryogenic Charge Sensing Readout

Since the charge sensor and the quantum dot are capacitively coupled, the Coulomb peak of the charge sensor is shifted by electronic charging events on the target dot at DC and by

mechanical vibration of the tube containing it at the mechanical frequency ω_m. These shifts produce a modulation in the current received at the drain. The sensitivity is maximized by biasing the charge sensor gate voltage at the set point, corresponding to the steepest slope of the conductance in the $G(V_g)$ plot in Fig. 6 (C). To perform high-sensitivity charge detection in our quantum dot nanomechanical system, we employ a cryogenic readout technique based on a charge sensor defined as a SQD as explained in Section 3.1.

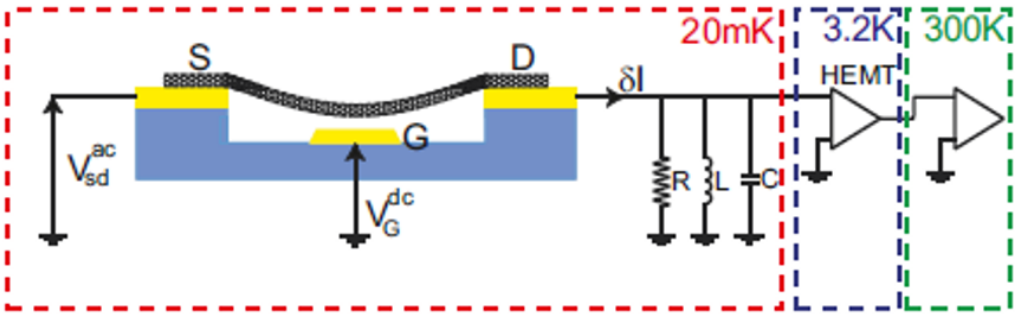

Figure 8: Cryogenic charge-sensing circuit.

To read out the signal, we apply an RF drive at a frequency:

$$f_{\mathrm{RLC}} = \frac{\omega_{\mathrm{RLC}}}{2\pi} = 1.25 \text{ MHz}.$$

Operation at a higher frequency reduces the readout noise. The modulated current through the nanotube is converted to a voltage by a resistor, so that it can be measured with a high-electron mobility transistor (HEMT).

To measure the signal, we use an RLC resonator at f_{RLC}, formed by an added inductor and the capacitance of the transmission line. This is necessary to measure the higher-frequency signals, since without it they would be suppressed by the RC filter formed by the resistor and the unavoidable capacitance of the transmission lines. The modulated signal is then first amplified using a HEMT amplifier at 3.5 K, followed by a room temperature amplifier at 300 K.

3.4 Charge Stability Diagrams

When a suspended CNT is tuned into a double quantum dot (DQD) configuration using local electrostatic gates, its charge stability diagram reveals a characteristic honeycomb pattern. This pattern arises from Coulomb blockade in each dot and their mutual capacitive coupling. Each hexagonal cell corresponds to a distinct charge configuration (N_L, N_R), where N_L and N_R are the electron occupations on the left and right dots, respectively. The boundaries between cells represent transitions where the chemical potential of one dot aligns with the Fermi level of the leads, allowing a single-electron tunneling event into or out of that dot [WGvdWK02].

In our device, DQD is defined electrostatically by gate voltages applied to the local bottom gates. We sweep gate voltages V_{g2} and V_{g4}, which primarily modulate the electrochemical potentials μ_L and μ_R of the left and right dots, respectively. The charge stability diagram measured in this two-dimensional gate space maps out regions of fixed charge occupancy, separated by sharp transition lines. Triple points occur when three charge states become degenerate—for example, (M, N), $(M+1, N)$, and $(M, N+1)$ all have the same total energy. At these points, all relevant states are energetically accessible, allowing current to flow through the DQD via tunneling.

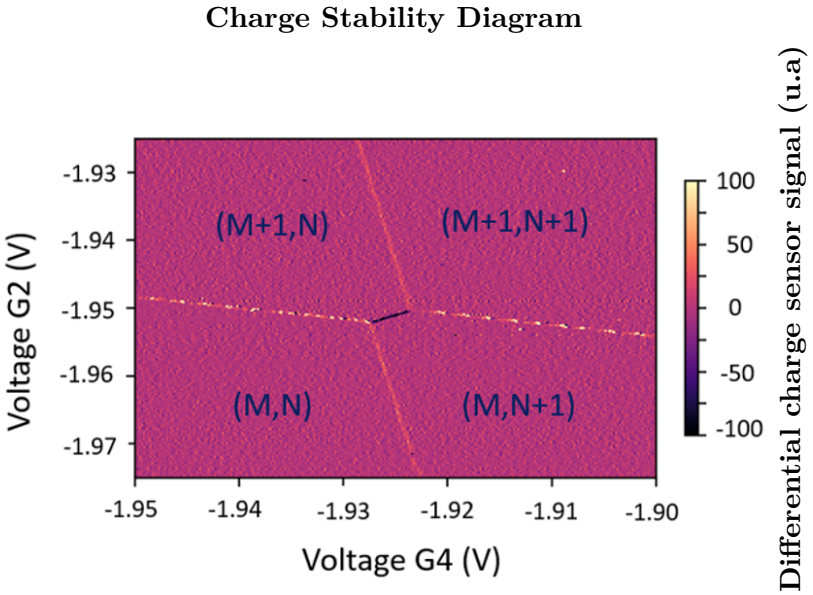

Figure 9: Charge stability diagram showing the characteristic honeycomb pattern of a double quantum dot. The labels (M, N), $(M+1, N)$, $(M, N+1)$, and $(M+1, N+1)$ indicate the electron occupation numbers of the two dots. The light-colored lines correspond to charging lines, where an electron is added to or removed from one of the dots, defining the boundaries between different charge configurations. The dark diagonal line is the ICT, where an electron moves between the two dots. The triple points occur exactly where two charging lines (one from each dot) and the ICT line intersect—these are the corners of the honeycomb cells where three charge states become degenerate. At these points, both dots are aligned with the Fermi levels of the leads, allowing electron exchange with the reservoirs. The color scale represents the differential charge sensor signal, defined as the pixel-to-pixel change in the charge sensor position across the diagram. Unlike transport measurements, which typically show only the triple points, this approach captures the full charge state boundaries.

The interdot charge transition (ICT) in a double quantum dot occurs along the boundary between charge states $(N+1, M)$ and $(M, N+1)$, where the total electron number remains fixed but an electron can tunnel between the two dots. At the degeneracy point (zero detuning), the system forms a coherent superposition of the two charge configurations, and the electron becomes delocalized across both dots. The width of the ICT quantifies the energy of the associated quantum dot.

3.5 Deep Learning Analysis

A custom deep learning model was developed in this project to learn and reproduce charge stability diagrams from gate-defined quantum dot devices. The model input consists of two components: (i) experimental charge stability diagrams measured as two-dimensional conductance maps versus gate voltages (gates 2 and 4 sweeps), and (ii) metadata containing voltages on neighboring gates (1, 3, 5). Together, these inputs encode the local charge configuration and the surrounding electrostatic environment, making them ideal input data for the model to learn from.

The model analyzes charge stability diagrams, by learning compact representations of their underlying physical features. It learns by comparing its generated diagrams to the original measurements and gradually improves through repeated exposure to examples. The trained model was able to reproduce key structural features of the diagrams, including charging and ICT lines, as well as triple points. A more detailed description of the model

architecture, training process, performance and limitations is provided in Appendix A.

This model will be further developed during my PhD with the group, with the aim of predicting gate voltage configurations to enable more efficient exploration of the parameter space and ultimately automate measurements. A second motivation is to identify correlations between charge stability diagram features and gate voltages. This is particularly valuable in complex regimes where visual interpretation becomes difficult. One such example is the blocked configuration, where the tunnel barriers to the leads are so high that the tunneling is strongly suppressed. In such regimes, energy levels of the QD can be detuned out of equilibrium.

4 Nano-Mechanical Thermal Motion Temperature Measurements

4.1 Nano-Mechanical Thermal Motion

For CNT resonators, the extremely low effective mass results in large zero-point motion amplitudes and correspondingly high amplitude thermal fluctuations, even at cryogenic temperatures [SLdBB18]. Despite this, detecting the thermal motion of such mechanical systems is challenging. At low temperatures, the average phonon occupation number becomes small, resulting in extremely weak displacement signals. Moreover, CNT resonators are highly sensitive to electrical and environmental noise, and conventional detection techniques often lack the sensitivity required to measure their motion without applying strong external driving.

The power spectral density (PSD) of a thermally driven harmonic oscillator exhibits a Lorentzian peak. Integrating the PSD over all frequencies yields the mean-square displacement, $\langle x^2 \rangle$ [MAM14].

According to the equipartition theorem, the average potential energy of the mode is given by

$$\frac{1}{2} m_{\text{eff}} \omega_m^2 \langle x^2 \rangle = \frac{1}{2} k_B T,$$

where m_{eff} is the effective mass of the CNT resonator, ω_m is the mechanical resonance frequency, and, k_B is the Boltzmann constant. This leads to

$$\langle x^2 \rangle = \frac{k_B T}{m_{\text{eff}} \omega_m^2}.$$

In the quantum limit, as $T \to 0$, the mechanical zero-point fluctuation amplitude is given by

$$x_{\text{zpf}} = \sqrt{\frac{\hbar}{2 m_{\text{eff}} \omega_m}},$$

where $\hbar$ is the reduced Planck constant [MAM14]. Hence, the intrinsic temperature of the mechanical mode can be inferred by measuring the PSD as a function of the cryostat temperature.

4.2 Temperature Dependence

Fig. 10 shows our measurement of the PSD of a CNT mechanical resonator at a cryostat temperature of 35 mK, exhibiting a Lorentzian profile centered at the resonant frequency. The plot shows a sharp resonance peak centered at approximately 164 MHz and it corresponds to the mechanical resonance frequency of the CNT resonator. The peak arises due to the thermally excited vibrations of the CNT. The maximum power spectral density

reaches about 1.5×10^{-15} W/Hz on resonance, and the total vibrational energy is quantified by the area under it. The sharpness (narrow width) of the resonance peak indicates a high quality factor (Q) of the CNT resonator. A higher Q means lower energy dissipation.

The Q for the mechanical resonance can be measured as

$$Q = \frac{f_0}{\gamma} = \frac{164.05 \times 10^6}{169} \approx 9.7 \times 10^5,$$

where f_0 is the resonance frequency and $\gamma = 169$ Hz is the linewidth (full width at half maximum).

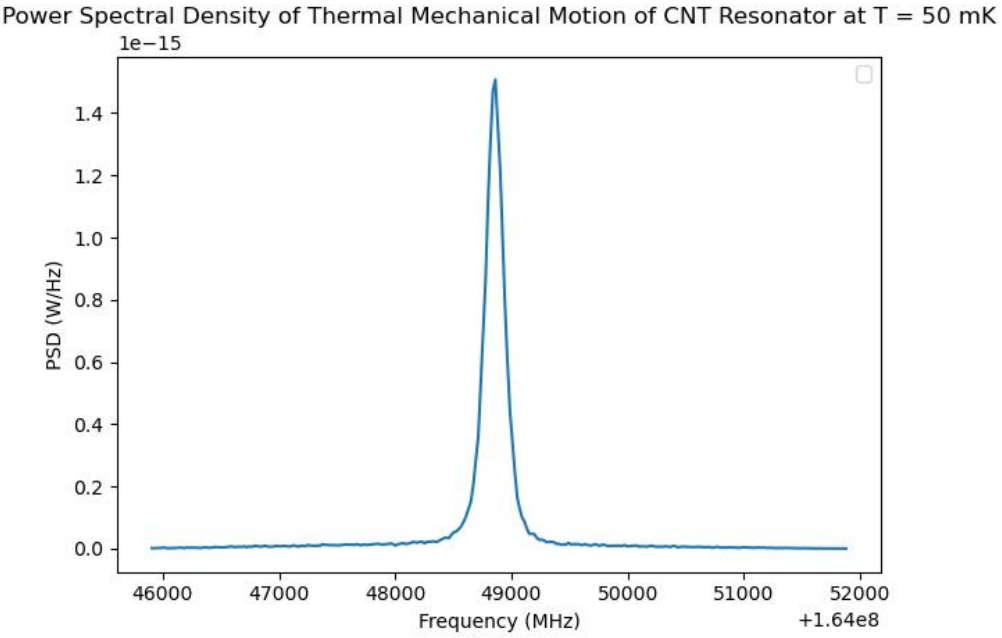

Figure 10: Lorentzian Power Spectral Density of CNT resonator at 50 mK.

Measuring the temperature of thermomechanical motion is important because temperature determines the average phonon occupation in the system. As the temperature is lowered, the phonon number decreases, and the system approaches the quantum regime. Tracking this behavior allows us to quantify the system's sensitivity in the low-phonon limit and assess how closely it approaches the Standard Quantum Limit (SQL), the fundamental bound on measurement precision set by quantum mechanics. Intuitively, the SQL is equivalent to measuring one phonon with a Signal-to-Noise Ratio (SNR) = 2 [MAM14].

We conducted thermomechanical motion measurements over a mode temperature range from 50 mK to 160 mK to study how the PSD amplitude changes with temperature and to quantify $\langle x^2 \rangle$ as described in Section 4.1. The integrated area under the curve (Fig. 11 (B)) does not scale linearly with temperature, as would be otherwise predicted theoretically. While the shape of the PSD remains consistent, its amplitude also deviates from linear temperature scaling (Fig. 11 (A)).

The most likely reason for this discrepancy is that the charge sensor sensitivity changes with temperature. To account for these variations, the sensor sensitivity was quantified using the conductance trace. As described in Section 3.3, the motion of the resonator is transduced via a nearby charge sensor. The displacement of the CNT modulates the electrostatic environment, which in turn modulates the current of the sensor. The charge sensor responds to this modulation through its conductance curve, $G(V_g)$. Importantly,

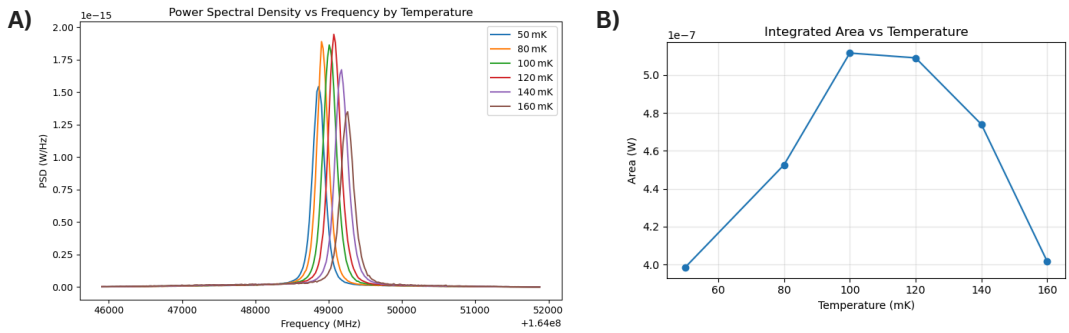

Figure 11: (A) Temperature-Dependent Lorentzian PSD of CNT resonator. (B) Integrated Area under the PSD.

the magnitude of the response depends on the slope of $G(V_g)$. When the slope is steep, even a small shift in gate voltage produces a large change in conductance, leading to high sensitivity. Conversely, when the slope is flatter, the same displacement produces a weaker response. More generally, the sensitivity of the charge sensor can vary between cooldowns and configurations due to factors such as the relative positioning of the sensor and the quantum dot, or changes in the capacitive coupling strength.

Therefore, the measured PSD reflects not only the amplitude of the mechanical motion but also the slope of the charge sensor conductance at the set point (the voltage at which the charge sensor gate is biased). To extract the sensitivity quantitatively, we measured the $G(V_g)$ for each PSD measurement. The $G(V_g)$ slope was initially extracted by applying a best-fit line to a range of data points around the set point, resulting in the PSD scaling. We scaled the PSD by the inverse square of the slope, since the PSD amplitude scales quadratically with charge sensitivity. However, the extracted slope showed an error that varied depending on how wide a range of data points was selected around the set point. The error bar on each slope was on the order of a few 10^{-3} S/V, corresponding to roughly 5-10% of the fitted value, rendering the method unreliable. To address this, a second approach was employed, in which the $G(V_g)$ was fitted using the Breit–Wigner resonance formula:

$$G_{BW} = \frac{2e^2}{h} \cdot \frac{(\hbar\Gamma)^2}{(\hbar\Gamma)^2 + \delta^2}, \tag{5}$$

where:

- G_{BW} is the conductance of the charge sensor,
- $\hbar\Gamma$ is the level broadening due to tunnel coupling,
- δ is the detuning between the quantum dot energy level and the Fermi level of the leads.

Due to a finite bias from thermoelectric effects in the transmission lines, which was not compensated to minimize noise, we fitted only the left half of the conductance curve where the set point is located, as shown in Fig. 12 (A). The corrected PSD is presented in Fig. 12 (C), with the corresponding area under the PSD shown in Fig. 12 (B).

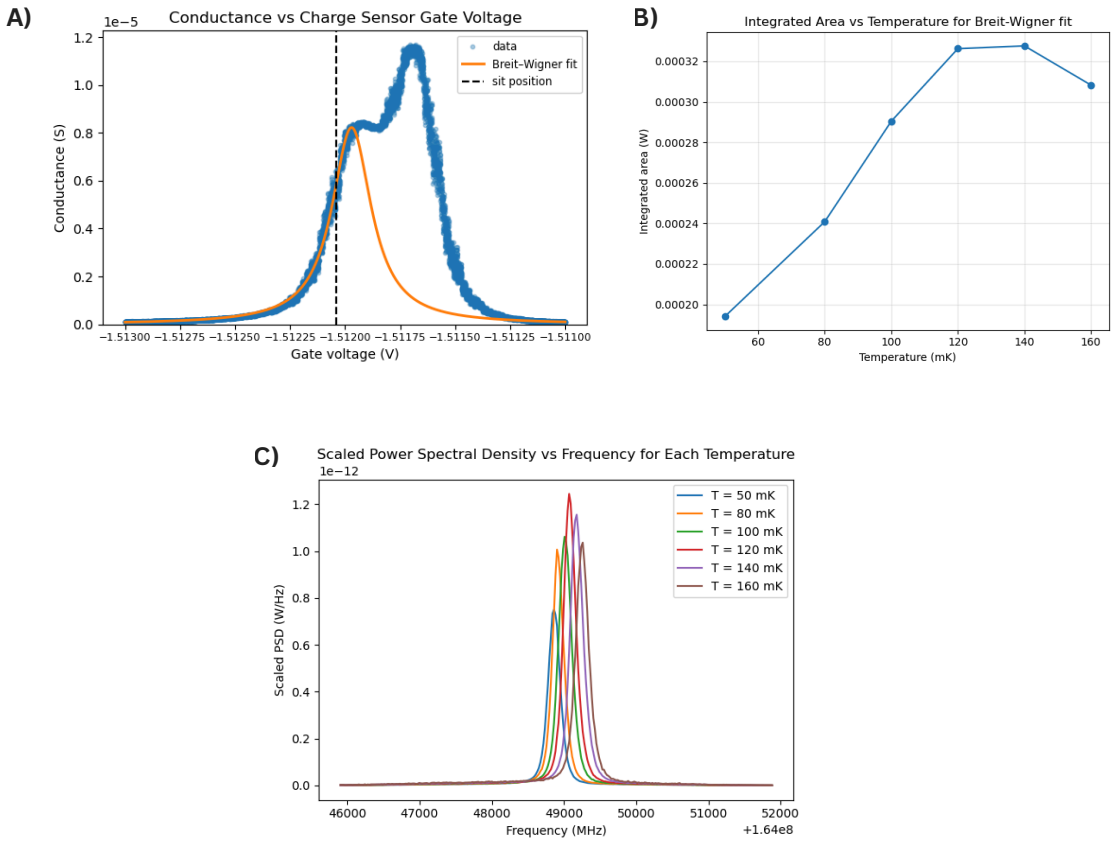

Figure 12: (A) Fit to charge sensor conductance using the Breit–Wigner function (left half of peak). (B) Integrated Area under the scaled PSD. (C) PSD scaled by the inverse square of the conductance slope.

Although this approach partially corrected for variations in sensitivity, the PSDs still did not scale linearly with temperature. This suggests that additional factors, such as variations in spatial coupling or quantum dot geometry with temperature, may influence the PSD in ways not fully captured by the slope of $G(V_g)$.

Nonetheless, this analysis provided useful insight for future experimental design. In particular, it highlighted that consistent scaling of the PSD with temperature requires a charge sensing configuration with well-controlled, temperature-independent sensitivity. Ensuring that the Coulomb peak used for sensing remains stable across temperatures would significantly improve the robustness of thermomechanical measurements. This can be achieved with a configuration where tunnel coupling dominates over thermal broadening at all temperatures.

Such a measurement is shown in Fig. 13 (A), presenting the PSD of the CNT resonator at various temperatures. The amplitude of thermal motion increases proportional to temperature. Integrating the PSD yields the mean-square displacement $\langle x^2 \rangle$, which also increases linearly with temperature, as shown in Fig. 13 (B). This measurement scales as theoretically expected because the Coulomb peak was fixed across all measurements. From this we can confidently infer the mode temperature to be at most around 50 mK for the current and previous measurement, since the measured displacement amplitude reliably reflects the thermal motion of the resonator. Here, we numerically calculate the phonon occupation number from the Bose-Einstein distribution:

$$\langle n_{\text{th}} \rangle \approx \frac{k_B T}{\hbar \omega_m} = \frac{1.38 \times 10^{-23} \times 0.050}{1.05 \times 10^{-34} \times 1.03 \times 10^{9}} \approx 6$$

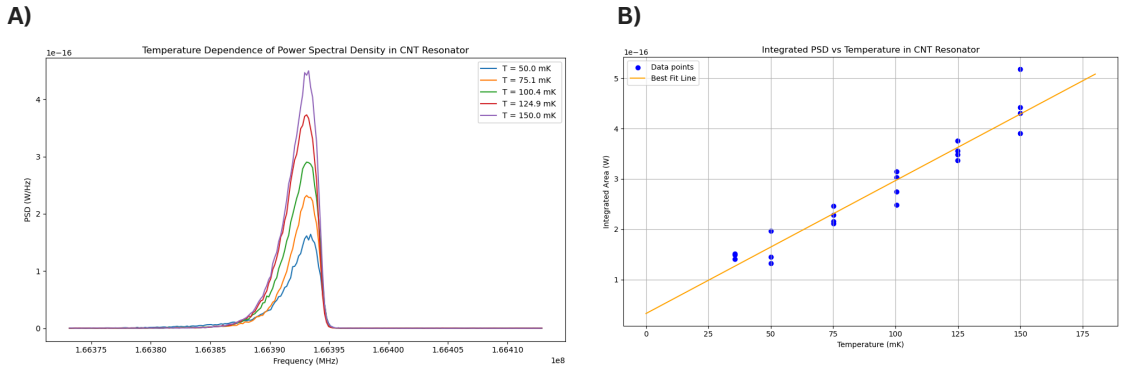

Figure 13: (A) PSD at different temperatures. (B) Extracted $\langle x^2 \rangle$ showing linear temperature dependence.

However, in this thermal resonance, we observe strong asymmetries that decrease with temperature in this measurement. These could arise from coupling to two-level systems (TLS). Fig. 14 (A) shows a single asymmetric PSD measurement, with its corresponding time–frequency spectral map in Fig. 14 (B). To analyze the origin of these asymmetries, we removed time intervals corresponding to frequency jumps away from the resonant frequency, as shown in Fig. 14 (D). Fig. 14 (C) shows persisting asymmetries in the lineshape that remain after accounting for these jumps, which may reflect intrinsic nonlinear behavior of the resonator. Nonlinear behavior in a mechanical resonator means that the resonator's restoring force is no longer a linear function of displacement.

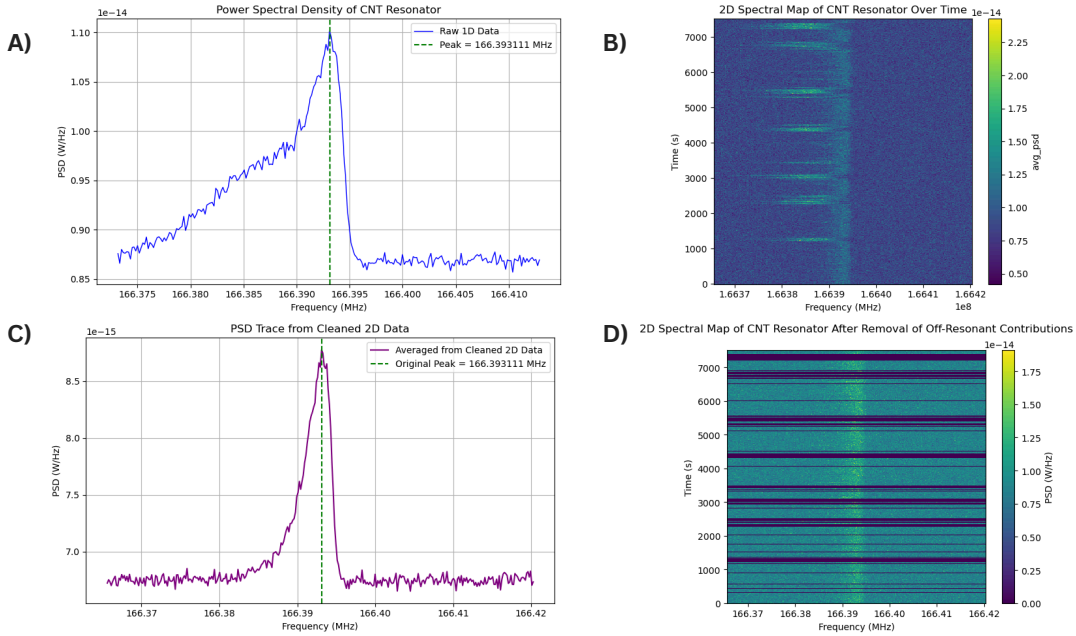

Figure 14: (A) Asymmetric PSD. (B) 2D spectral map showing frequency jumps. (C) Residual asymmetry. (D) 2D spectral map after removal of off-resonance fluctuations.

We did a more extensive analysis on an equivalent device, which revealed clear signs of nonlinearity, and hence the residual asymmetry is interpreted as such. This nonlinearity is likely linked to the specific charge sensing configuration used: the wider, tunnel-coupled peak is less sensitive and hence to see the thermal motion, the target dot has to be placed very close to the charge sensor dot, this induces a coupling of the mechanical mode to TLS, which creates a nonlinearity [SB23, Pis18]. Once properly controllable, such nonlinearities could be useful in the future for preparation of non-Gaussian quantum states of mechanical motion, with application in sensing and quantum information processing.

5 Conclusions

We investigated thermomechanical motion in suspended CNT resonators at millikelvin temperatures, achieving phonon occupation numbers below 10. We performed a CNT CVD growth yielding seven good devices, each with a single ultra-clean, semiconducting, single-walled nanotube suspended across the gate array, as verified through subsequent probing. The devices were designed to incorporate quantum dots and an integrated charge sensor for cryogenic radio-frequency readout.

We measured Lorentzian power spectral densities of the mechanical resonance and examined their temperature dependence. While charge sensor sensitivity was considered as a contributing factor to deviations from ideal scaling, it did not fully account for the observed behavior.

In configurations with a stable conductance response to the charge sensor gate voltage across temperatures, the mechanical motion scaled linearly with temperature, as expected. However, we also observed spectral asymmetries and features likely linked to TLS coupling–induced nonlinearity. These results offer insight into the challenges of precision sensing in low-phonon nanomechanical systems and inform future approaches to achieving consistent, high-sensitivity measurements.

Lastly, a deep learning model was developed using experimental charge stability diagrams and gate voltage metadata as input. The model learns compact representations of the underlying physical features and successfully reconstructs structural patterns. It will be further developed during my PhD to predict gate configurations for automated measurements and to identify correlations between gate voltages and charge states, particularly in regimes where visual interpretation is challenging.

Bibliography

[AC16] Abbott R.-Abbott T. D. Abernathy M. R. Acernese F. Ackley K. Adams C. Adams T. Addesso P. et al. (LIGO Scientific Collaboration Abbott, B. P. and Virgo Collaboration). Observation of gravitational waves from a binary black hole merger. *Physical Review Letters*, 116:061102, Feb 2016.

[AY23] Lim Heng-Siong Md Saad Mohamad Hanif Alaghbari, Khaled A. and Yik Seng Yong. Deep autoencoder-based integrated model for anomaly detection and efficient feature extraction in iot networks. *IoT*, 4(3):345–365, Aug 2023.

[CB12] Eichler A. Moser-J. Ceballos G. Rurali R. Chaste, J. and A. Bachtold. A nanomechanical mass sensor with yoctogram resolution. *Nature Nanotechnology*, 7:301–304, Apr 2012.

[CGS12] Meerwaldt Harold B. Venstra Warner J. van der Zant Herre S. J. Castellanos-Gomez, Andres and Gary A. Steele. Strong and tunable mode coupling in carbon nanotube resonators. *Physical Review B*, 86:041402, Jul 2012.

[CMK21] Erica J. Sturm Deyu Lu Andreas Weichselbaum Kipton Barros Cole Miles, Matthew R. Carbone and Robert M. Konik. Machine learning of kondo physics using variational autoencoders and symbolic regression. *Phys. Rev. B*, 104:235111, Dec 2021.

[CR98] A. N. Cleland and M. L. Roukes. A nanometre-scale mechanical electrometer. *Nature*, 392:160–162, Mar 1998.

[EALK15] Gary A. Steele Kasper Grove-Rasmussen Jesper Nygård Karsten Flensberg Edward A. Laird, Ferdinand Kuemmeth and Leo P. Kouwenhoven. Quantum transport in carbon nanotubes. *Reviews of Modern Physics*, 87:703, Jul 2015.

[FPB21] A.N. Cleland F. Pistolesi and A. Bachtold. Proposal for a nanomechanical qubit. *Phys. Rev. X*, 11:031027, Aug 2021.

[FVA22] Jorge Tabanera Kushagra Aggarwal Léa Bresque-Federico Fedele Federico Cerisola G. A. D. Briggs Janet Anders Juan M. R. Parrondo Alexia Auffèves Florian Vigneau, Juliette Monsel and Natalia Ares. Ultrastrong coupling between electron tunneling and mechanical motion. *Physical Review Research*, 4(4):043168, Dec 2022.

[HL04] Woodson Mike Smalley Richard Huang, Shaoming and Jie Liu. Growth mechanism of oriented long single walled carbon nanotubes using "fast-heating" chemical vapor deposition process. *Nano Letters*, 4(6), May 2004.

[Iij91] Sumio Iijima. Helical microtubules of graphitic carbon. *Nature*, 354:56–58, Nov 1991.

[JZ08] Kim Kwanpyo Jensen, K. and A. Zettl. An atomic-resolution nanomechanical mass sensor. *Nature Nanotechnology*, 3:533–537, Jul 2008.

[MA20] Lennon D. T. Kirkpatrick J. van Esbroeck N. M. Camenzind L. C. Yu Liuqi Vigneau F. Zumbühl D. M. Briggs G. A. D. Osborne M. A. Sejdinovic D. Laird E. A. Moon, H. and N. Ares. Machine learning enables completely automatic tuning of a quantum device faster than human experts. *Nature Communications*, 11:4161, Aug 2020.

[MAM14] Tobias J. Kippenberg Markus Aspelmeyer and Florian Marquardtn. Cavity optomechanics. *Reviews of Modern Physics*, 86:1391, Dec 2014.

[MB13] Güttinger J. Eichler A. Esplandiu M. J. Liu D. E. Dykman M. I. Moser, J.

and A. Bachtold. Ultrasensitive force detection with a nanotube mechanical resonator. *Nature Nanotechnology*, 8:493–496, Jun 2013.

[MJBM05] N. Mason J. M. Chow M. J. Biercuk, S. Garaj and C. M. Marcus. Gate-defined quantum dots on carbon nanotubes. *Nano Lett.*, 5(7):1267–1271, Jul 2005.

[MSN25] Yuksel M. Hitchcock O. A. Lee N. R. Mayor F. M. Jiang W. Roukes M. L. Maksymowych, M. P. and A. H. Safavi-Naeini. Frequency fluctuations in nanomechanical resonators due to quantum defects. *arXiv preprint arXiv:2501.08289*, Jan 2025.

[NY23] Kwai-Kong Ng and Min-Fong Yang. Unsupervised learning of phase transitions via modified anomaly detection with autoencoders. *Phys. Rev. B*, 108:214428, Dec 2023.

[PAW03] R. Martel P. Avouris, J. Appenzeller and S. J. Wind. Carbon nanotube electronics. *Proc. IEEE*, 91(11):1772–1784, Nov 2003.

[Pis18] Fabio Pistolesi. Bistability of a slow mechanical oscillator coupled to a laser-driven two-level system. *Physical Review A*, 97:063833, Jun 2018.

[SB23] De Bonis S. L. Møller C. B. Tormo-Queralt R. Yang W. Urgell C. Stamenic B. Thibeault B. Jin Y. Czaplewski D. A. Pistolesi F. Samanta, C. and A. Bachtold. Nonlinear nanomechanical resonators approaching the quantum ground state. *Nature Physics*, 19:1340–1344, Jun 2023.

[SLdBB18] W. Yang C. Samanta-A. Noury J. Vergara-Cruz Q. Dong Y. Jin S. L. de Bonis, C. Urgell and A. Bachtold. Ultrasensitive displacement noise measurement of carbon nanotube mechanical resonators. *Nano Letters*, 18(8):5324–5328, Aug 2018.

[SMPW22] D. B. Lee J. W. Choi H. Y. Kwon S. M. Park, H. G. Yoon and C. Won. Optimization of physical quantities in the autoencoder latent space. *Scientific Reports*, 12:9003, May 2022.

[SSM25] Joshua Folk Eran Sela Sarath Sankar, Matan Lotem and Yigal Meir. Back-action effects in charge detection. Mar 2025.

[WGvdWK97] J. M. Elzerman T. Fujisawa S. Tarucha W. G. van der Wiel, S. De Franceschi and L. P. Kouwenhoven. Electron transport in quantum dots. In L. L. Sohn, L. P. Kouwenhoven, and Gerd Schön, editors, *Mesoscopic Electron Transport*, volume 345 of *NATO ASI Series E: Applied Sciences*, page 105. Springer, 1997.

[WGvdWK02] J. M. Elzerman T. Fujisawa S. Tarucha W. G. van der Wiel, S. De Franceschi and L. P. Kouwenhoven. Electron transport through double quantum dots. *Rev. Mod. Phys.*, 75:1, Dec 2002.

A Deep Learning Approach for Charge Stability Diagrams Analysis

Deep learning can be understood by starting with the simplest building block of neural networks: a single neuron. A neuron takes in numerical inputs, applies weights and a bias producing an output as shown in Fig. 15 . When many neurons are combined, they form a layer, and when these layers are stacked, they create the powerful architectures we know as neural networks. Extending this idea, convolutional neural networks (CNNs) arrange neurons in a way that captures spatial patterns, making them especially effective for images.

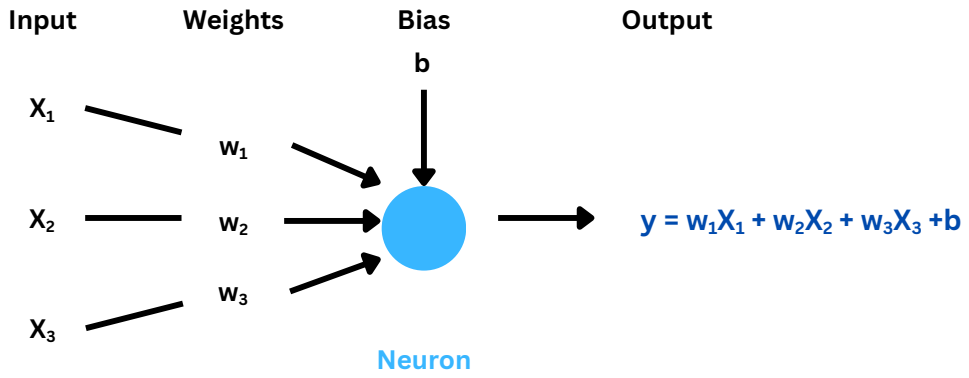

Figure 15: Illustration of a single artificial neuron. The neuron receives three inputs x_1, x_2, x_3, each multiplied by a corresponding weight w_1, w_2, w_3. The output y, computed as a weighted sum of the inputs plus the bias, forms the basic unit of computation in a neural network.

An autoencoder architecture (Fig. 16) consists of three principal components: the encoder, which maps the high-dimensional input data into a lower-dimensional latent representation; the bottleneck, which constitutes this compressed latent space and captures the most important features of the input distribution; and the decoder, which reconstructs the latent representation into an approximation of the original input. Autoencoders built with CNNs use this principle to learn compact, efficient representations of data by encoding inputs into a smaller latent space.This approach could serve as a powerful predictive tool for charge stability diagrams, first to automate measurements, and secondly to identify correlations within the latent representation between features of the charge stability diagrams and the gate voltages.

This strategy has already proven to be powerful in condensed-matter contexts. For example, autoencoders have learned latent variables that accurately predict phase transitions in previously uncharacterized systems [NY23], enabled the optimization of spin textures in simulated two-dimensional chiral magnetic systems through latent-space exploration [SMPW22], and identified emergent electronic phenomena in strongly correlated models [CMK21].

Furthermore, machine learning has been employed to accelerate algorithmic searches for specific electron transport features in gate-defined quantum dot devices, achieving results 70 minutes faster than a human expert and up to 180 times faster than automated random parameter searches [MA20].

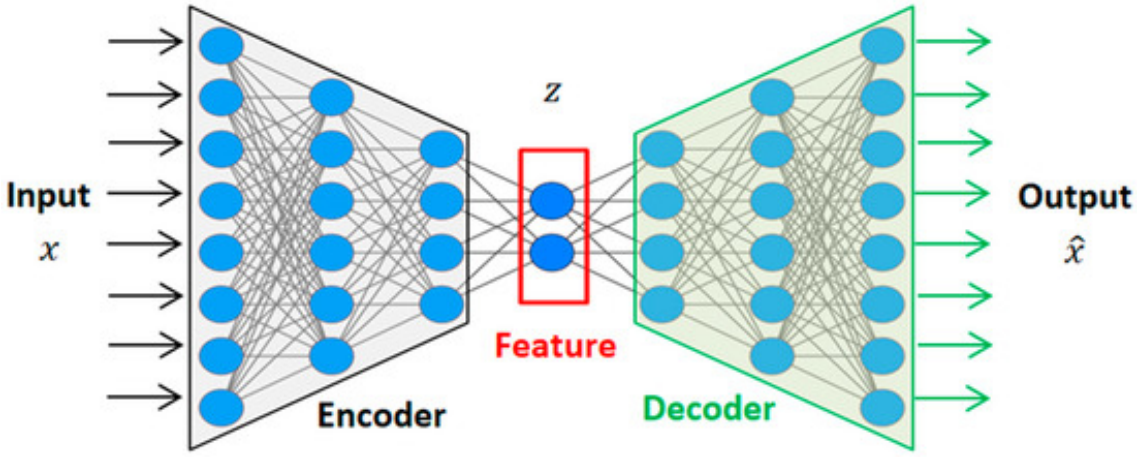

Figure 16: Figure adapted from K.A.Alaghbari et al. [AY23] shows a schematic of an autoencoder consisting of fully connected layers. The input x is processed by the encoder, which compresses it into a low-dimensional latent representation z. This compact feature captures essential information about the input. The decoder reconstructs the input as $\hat{x}$ from z.

The encoder CNN input consists of charge stability diagrams that were divided into tiles where each tile spans 1 mV and each pixel corresponds to 10 µV, which is the typical resolution of the ICT line. The encoder applies convolutional layers that detect relevant features such as charge transition lines and Coulomb blockade signatures. Nonlinearity is introduced via rectified linear unit (ReLU) activation. Batch normalization layers stabilize training by rescaling intermediate signals and dropout layers mitigate overfitting to experimental noise. In parallel, standardized gate-voltage metadata are processed through fully connected layers, ensuring that parametric information is learned alongside image features. With increasing depth, spatial resolution is reduced, compressing higher-order correlations into compact feature representations. The result is 32 latent vectors that jointly encode both spatial and parametric dependencies.

The decoder reverses the encoding process, using upsampling and convolutional layers to reconstruct the input, with a final sigmoid layer constraining outputs to $[0, 1]$ to preserve numerical stability.

The network is trained with a hybrid loss function:

$$L = \alpha L_{\text{MSE}} + \beta(1 - \text{SSIM}). \tag{6}$$

where α and β are weighting coefficients.

The mean squared error (MSE) term is given by:

$$L_{\text{MSE}} = \frac{1}{N}\sum_{i=1}^{N}(y_i - \hat{y}_i)^2, \tag{7}$$

which enforces pixel-wise accuracy between predicted $\hat{y}_i$ and experimental y_i .

The structural similarity index (SSIM) is expressed as:

$$\text{SSIM}(x, y) = \frac{(2\mu_x\mu_y + C_1)(2\sigma_{xy} + C_2)}{(\mu_x^2 + \mu_y^2 + C_1)(\sigma_x^2 + \sigma_y^2 + C_2)}, \tag{8}$$

where μ_x, μ_y are local means, σ_x^2, σ_y^2 variances, and σ_{xy} the covariance. C_1 and C_2 are stabilization constants. SSIM emphasizes preservation of structural features and contrast.

The model learns by comparing its output to the original charge stability diagram and calculating the loss. This loss is then used to adjust the internal weights and biases of the network. Through backpropagation, each layer receives feedback on how much it contributed to the error, and the optimizer makes small corrections to the weights and biases to reduce that error. Repeating this process over many examples gradually improves the network's ability to reproduce the correct physical features of the diagrams.

The trained autoencoder successfully reconstructs experimental charge stability diagrams, capturing the spatial features correctly. The model was able to reconstruct the ICT lines, recognize triple points, and even hysteresis in charging lines, which may correspond to charge traps. The loss reached 0.013, indicating how closely the autoencoder's output matches the input.

The current model exhibits several limitations that affect reconstruction quality. First, repeated up- and down-sampling in the convolution layer operations resulted in the loss of information at the corners of each tile. This can be fixed by tuning the layer's parameters. Second, the latent dimension was restricted to 32, which enforces strong compression but may overly constrain the representational capacity. Higher-dimensional latent spaces are generally known to preserve more subtle features but are more computationally expensive. Finally, the model does not scale conductance values consistently across tiles, despite capturing the main structural features of the images. This issue is likely linked to the normalization strategy, as data was normalized per tile rather than across the full measurement, potentially limiting generalization. These challenges inform future model tuning for this type of data, guiding improvements in architectural design and normalization strategies.

The two directions for future work are: first, reconstructing approximate features of charge stability diagrams using only the applied gate voltages and temperature; and second, extracting correlations by comparing the model's learned representations with COMSOL simulations of the band diagram.